Batteries & Supercaps

Research Article
doi.org/10.1002/batt.202100314

**Chemistry
Europe**
European Chemical
Societies Publishing

www.batteries-supercaps.org

All-Solid-State Flexible Symmetric Supercapacitor Based on Morphology Oriented Amorphous Cu–Co–B Alloy Nanosheets for Energy Storage

Javed Muhommad,[a] Lakshya Kumar,[a] Purna K. Baruah,[b] Manash R. Das,[b] and Sasanka Deka*[a]

Metastable amorphous alloys having 2-dimensional morphology are expected to be an excellent electrode materials for supercapacitors because of their defect rich nature, high degree of compositional as well as topological disorder and internal stresses. Herein, we investigated and demonstrated a new series of Cu–Co–B amorphous alloy nanosheets for energy storage. A clear and significant energy storage improvement by this Cu–Co–B nanosheets over the state-of-the-art materials and flexible devices are manifested. Among the as-synthesized materials, $CuCo_2B$ nanosheets exhibits an excellent specific capacity of 3503.6 F g^{-1} (389.2 mAh g^{-1}) and a 99% (at 50 A g^{-1}) retention rate after 3000 cycles. An all-solid state flexible symmetric Cu–Co–B | [EMIM][BF$_4$] supercapacitor device (0–180° bending, 2.5 V) demonstrates a high energy density of 90.2 Wh kg^{-1}, specific capacity (289.2 mAh g^{-1}), power density (4623.6 W kg^{-1}) and prolonged cycling stability (89%) and Coulombic efficiency (104%) over 10000 charge-discharge cycles.

Introduction

Advanced electrochemical energy storage (EES) devices have the potential to make a major contribution to the implementation of sustainable and renewable energy because of their miniaturization but yet powerful characteristics.[1] These unprecedented advantages of EES are benefited from the fact that both electrical and chemical energy share the same carrier, the electron. In this scenario electrochemical supercapacitor (SC) are alternative to many high-efficiency EES devices in many instances due to high-power density, cycling stability, fast charging-discharging (fast redox reaction kinetics), easy designing and environmentally friendly characteristics of the former one.[2] The SC materials are expected to have high energy and power density, high capacitance and long cycling life; and they are often divided into three categories now-a-days (electric double layer capacitor, EDLC; pseudocapacitor; and battery-type SC) based on their charge-storage mechanisms.[3]

In recent years, nanostructures of various materials (Nb_2O_5, RuO_2, Co_3O_4, IrO_2, MnO_2, layered double hydroxides (LDHs), metal phosphides, metal carbides/nitrides (MXene), etc.) and exotic morphologies (spherical nanoparticles, nanotubes, nanosheets, hierarchical structures, etc.) have been investigated as pseudocapacitor as well as battery-type SC, because their advantages over EDLC.[4] Very fast kinetics of redox reaction and/or diffusion-controlled behavior are observed based on these types of SC materials.[3a,5] Interestingly, battery materials engineered at the nanoscale often found to exhibit "extrinsic" pseudocapacitance.[3] They are good volunteers to be used as electrode material to fabricate a flexible, cheap and rolled up device to overcome the issue of energy-power density, fast charging–discharging, and ease of synthesis.[6] Among the nanostructures, two-dimensional (2D) nanosheets (NSs) are found to be unique in energy storage applications due to their ultra-thin structure, high surface-to-volume ratio, shortened ion diffusion distance and it facilitates easy electron transportation.[5b,7] However, the exploration of electrode materials with higher performance and low cost for SCs is still of great importance and challenging.

In this scenario, metastable amorphous alloys with 2D morphology could be highly promising in the field of SCs because of their defect rich nature.[8] These materials exhibit a high degree of compositional as well as topological disorder and internal stresses, due to which they are expected to show better charge storage characteristics than many crystalline materials. Amorphous materials with high porosity and surface area increase the interface area between electrode and electrolyte for effective ion transportation and redox reaction, and large numbers of defects increase the active sites. Based on these advantages a few numbers of metal-boron (M–B) amorphous alloys have been synthesized successfully using mainly chemical reduction method and explored for SC application. Zhang et al. developed $Ni_{47.5}Co_{20.4}B_{32.1}$ amorphous alloy powder which exhibits a pseudocapacitance with 1310 F g^{-1} at 1.5 A g^{-1} in the 6 M KOH electrolyte.[9] Chen et al.

[a] J. Muhommad, L. Kumar, Dr. S. Deka
Nanochemistry Laboratory,
Department of Chemistry
University of Delhi
North Campus, Delhi-110007, India
E-mail: sdeka@chemistry.du.ac.in
[b] Dr. P. K. Baruah, Dr. M. R. Das
Advanced Materials Group,
Materials Sciences and Technology Division
CSIR-North East Institute of Science and Technology
Jorhat 785006, Assam, India

Supporting information for this article is available on the WWW under
https://doi.org/10.1002/batt.202100314

reported high-performance (2226.96 F g^{-1}) nickel-cobalt-boron material for an asymmetric supercapacitor with a high energy density (66.40 Wh kg^{-1}). Interestingly, transition metal ratio and crystallinity of the final material greatly affect the performance of the cell in such cases.[10] Amorphous Co–Fe–B//active carbon asymmetric supercapacitor on 3D Ni-foam substrate displays excellent long-term stability and the capacitance increase 26% after 5000 cycles.[11] Redox tuning in crystalline and electronic structure of bimetal–organic frameworks derived cobalt/nickel boride/sulphide system offered faradaic capacitance (1281 F g^{-1} at 1 A g^{-1}), high rate performance (802.9 F g^{-1} at 20 A g^{-1}), and 92.1% cycling stability after 10000 cycles.[12] Recently, a flexible and wearable electrode based on the hierarchical structure of RGO-coated cotton fabric with amorphous Co–Ni–B alloy was reported with an optimum specific capacitance of 313.9 F g^{-1} at 5 mV s^{-1}, and 85% stability after 3000 cycles.[13] However, the applications of the amorphous transition metal borides (TMB) are not only confined to charge storage, but also extended to lithium storage, and electrocatalytic water splitting reactions.[14]

Notably only a few reports are seen on the study of TMB on SC application as stated above where efforts are still required for extremely high-performance supercapacitor material and devices. Out of various geometries of supercapacitor devices, flexible geometry with extreme bending, twisting, and foldable features are considered as one of the much-sought devices in present and future days. These flexible devices should be usable at high operating voltage, without the effect of deformation and should offer excellent capacitance, stability, energy and power density. Therefore, rational design and preparation of a new TMB material to overcome the problems for SC application have been the aim of this study. A combined approach is made by introducing Cu ions in the TMB system and making ultrathin 2D NSs for more aggressive Faradic redox reactions during charging-discharging. Herein, a novel 2D Cu–Co–B ultrathin NSs amorphous alloy is demonstrated for the first time, which is produced by a simple facile one pot chemical reduction method for SC application. The as-synthesized nanostructures provided the SC with a high specific capacity of 389.2 mAh g^{-1} (3503.6 F g^{-1}) and a 99% retention rate after 3000 cycles in 6 M KOH. Moreover, the assembled all-solid-state symmetric flexible SC (CuCo$_2$B//CuCo$_2$B) device in [EMIM][BF$_4$] electrolyte demonstrated a high energy density of 90.2 Wh kg^{-1}, power density of 4623.6 W kg^{-1}; and superlong cycling stability (89%) and high coulombic efficiency over 10000 charge-discharge cycles. This novel Cu–Co–B TMB NSs and the all-solid-state symmetric flexible SC offered excellent energy storage properties which are far exceeded over other reported SCs till date (see comparison Tables S4 and S7).

Results and Discussion

Facile synthesis of amorphous Cu–Co–B NSs was performed using a one-step synthesis method. At the beginning stage, metal (Cu^{2+} and Co^{2+}) acetates were converted to hydroxide as KOH was added to the metal salt solution, which helped the hydrolysis reaction less vigorous in reduction process during

the addition of NaBH$_4$. This step of the reaction helps to form certain morphology i.e., nanosheets in the present case in facial way. In 1998, Chen carried out exclusive studies on the reaction mechanism and kinetics for the preparation of TMB by chemical reduction method.[15] The BH$_4^-$ ions reduced the metal ions to their zero oxidation states and form HBO$_2$ and H$_2$ gas in an aqueous solution. BH$_4^-$ again undergo self-reduction to form B atoms depending on the pH of the solution (pH > 9). Finally, TMB are formed by the interaction of the metal (Cu, Co in present case) and boron atoms produced by a reaction which is induced by the metal atoms in solution [Eqs. (S1a)–(S3)].[9,15]

Structure and morphology analysis

The XRD patterns of the as-synthesised samples are shown in Figure 1(a). The XRD patterns demonstrate that all CCB samples present a single broad peak centered around $2\theta = 44°$–$45°$, confirming the amorphous nature of the Cu–Co–B materials. Similar XRD patterns have been reported in the literature for other TMB samples.[9–11] The formation of Cu–Co–B was further investigated by using FT-IR spectra (Figure S1). Apart from surface adsorbed water O–H vibration band, bending vibrations of H$_2$O and B–O bands (Figure S1a); Co–B and Cu–B vibration bands are clearly seen in the enlarged spectra (Figure S1b). The IR peaks at 400–600 cm^{-1} are attributed to the formation of the Co–B and Cu–B bonds in the alloys.[10,16] Furthermore, the result indicated that the used acetate counter ion (in metal complex) has been removed. All the samples show type IV and HI type of hysteresis loop (Figure 1b). The multipoint BET plot in nitrogen adsorption desorption isotherm gives a surface area of 98.62, 85.42 and 91.27 m^2 g^{-1}, and a pore radius of 4.46, 1.8 and 1.8 nm, for CCB1, CCB2 and CCB3, respectively. The pore volumes were found be nearly 0.34 cm^3 g^{-1} for all three samples.

Low resolution transmission electron microscopy (TEM) images of CCB1, CCB2 and CCB3 are compared in Figure 1(c–e). All samples are found to be of nanosheet morphology with very thin and transparent topology. The thickness of the nanosheets is determined using AFM and discussed in a later section. Under FESEM analyses, it is seen that those transparent nanosheets in CCB1 are interconnected; they first formed thick sheets and then formed a highly open 3D hierarchical structure (Figure 1f). HRTEM imaging is performed, however due to its amorphous nature no lattice fringes are visible in the sample (insets of Figures 1c–e and S2). Additionally, 2-dimensional Fast Fourier Transform (2D-FFT) analysis on these HRTEM images are done to see if any diffraction rings or patterns are present. However, supporting the initial data, no rings or spots are seen under 2d-FFT analyses (insets in Figure S2), confirming the amorphous nature of CCB samples. FESEM images of other samples are shown in Figure S3. Thus, the amorphous phase leads to more long-range distorted structure with more defects, which are expected to be beneficial for large electrochemically active surface area. The elemental mapping using SEM-EDS confirmed the chemical composition of the as-prepared sample (Figure 1g–k). It is found that the distribution of Cu, Co, and B
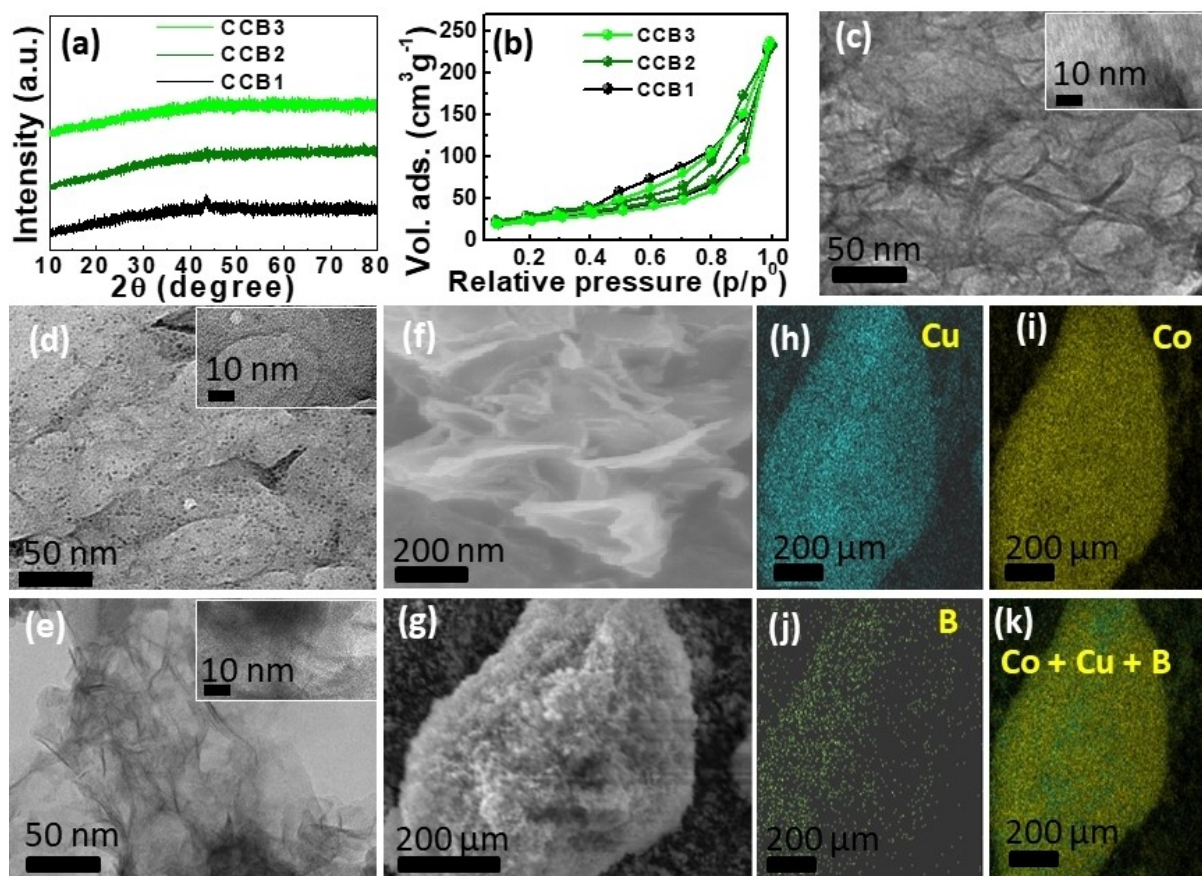
Figure 1. Structural and morphological characterizations of Cu–Co-B. a) XRD patterns of all as-synthesised compositions. b) BET isotherms of CCB1, CCB2 and CCB3 sample recorded at 77 K. c–e) Low-magnification TEM images of CCB1, CCB2, and CCB3 NSs, respectively. Insets: corresponding HRTEM images. f) FESEM image of CCB1 NSs. G–k) SEM-EDS elemental mapping of CCB1.

over the entire region is uniform for CCB1, corroborating a homogeneous phase of $CuCo_2B$. The SEM-EDAX analysis ensured that the chemical compositions of all Cu–Co–B samples are found to be same as fed during the synthesis (Figure S4). Thus, this results in the formation of alloy particles and ruled out the occurrence of any non-homogeneous nanostructures. In addition, inductively coupled plasma mass spectrometry (ICP-MS) measurement was carried out on CCB1 sample, which showed nearly 1:2 of Cu:Co elemental ratio (Table S1).

Atomic force microscopy (AFM) imaging was performed to elucidate the topography and the thickness of the as-prepared Cu–Co–B nanosheets. A rough surface with the typical topography of nanosheets is seen under AFM measurement (Figure 2a and b). The average height of single–single particles in line scan mode (of a much-diluted sample) is found to be in the range of 8–16 nm (Figure 2c). Interesting surface chemistry, chemical states and bonding in the as-prepared CCB1 sample was elucidated using XPS analyses. At first, elemental state of each constituent elements, viz. Cu^0 (932.61 and 952.47 eV, $\Delta = 18.86$ eV),[17] Co^0 (778.2 and 793.53 eV)[17] and B^0 (188.20 eV)[17] are observed and this corroborated the alloy phase of Cu–Co–B NSs (Figure 2d–f). In addition, oxidized states of these constituent elements were also observed in CCB1. The deconvoluted

spectrum of Cu 2p suggests the existence of Cu $2p_{3/2}$ (934.58 eV), Cu $2p_{1/2}$ (954.75 eV), and two shake-up satellite peaks (944.13 and 962.75 eV) for Cu^{2+} (Figure 2d).[18] Similarly, cobalt ions (Co^{2+}, Co^{3+}) are observed along with their satellite peaks (Figure 2e). The deconvoluted spectrum of Co 2p suggests the existence of Co $2p_{3/2}$ (779.91 and 781.40 eV), Co $2p_{1/2}$ (795.76 and 797.47 eV), and two shake-up satellite peaks (785.95 and 802.55 eV).[11,18] Moreover, a strong B–O signal at 191.50 eV is seen in B1s spectrum (Figure 2f).[10,11,14b] These oxidized states of the elements may result from the surface oxidation of the nanostructure. However, these oxide impurities are beyond the XRD detection limit and are limited exclusively to the surface, clearly indicating they hardly impact the energy storage activity, and they may be considered as mere spectators. Therefore, an additional XPS measurement has been performed after in-situ surface cleaning of the CCB1 sample using Ar^+ sputtering (135 s) to understand the actual elemental states below the oxide layer, which has not been studied earlier for any other TMBs. The wide scan XPS survey spectra of both fresh and sputtered samples are compared in Figure S5. It is clearly observed that, in-situ surface cleaning completely eliminated the Cu–O interaction original peak in the sputtered sample, leaving behind only Cu^0 peaks (Figure 2g).[17] Similarly, the original Co^{3+} peaks were also completely eliminated, and
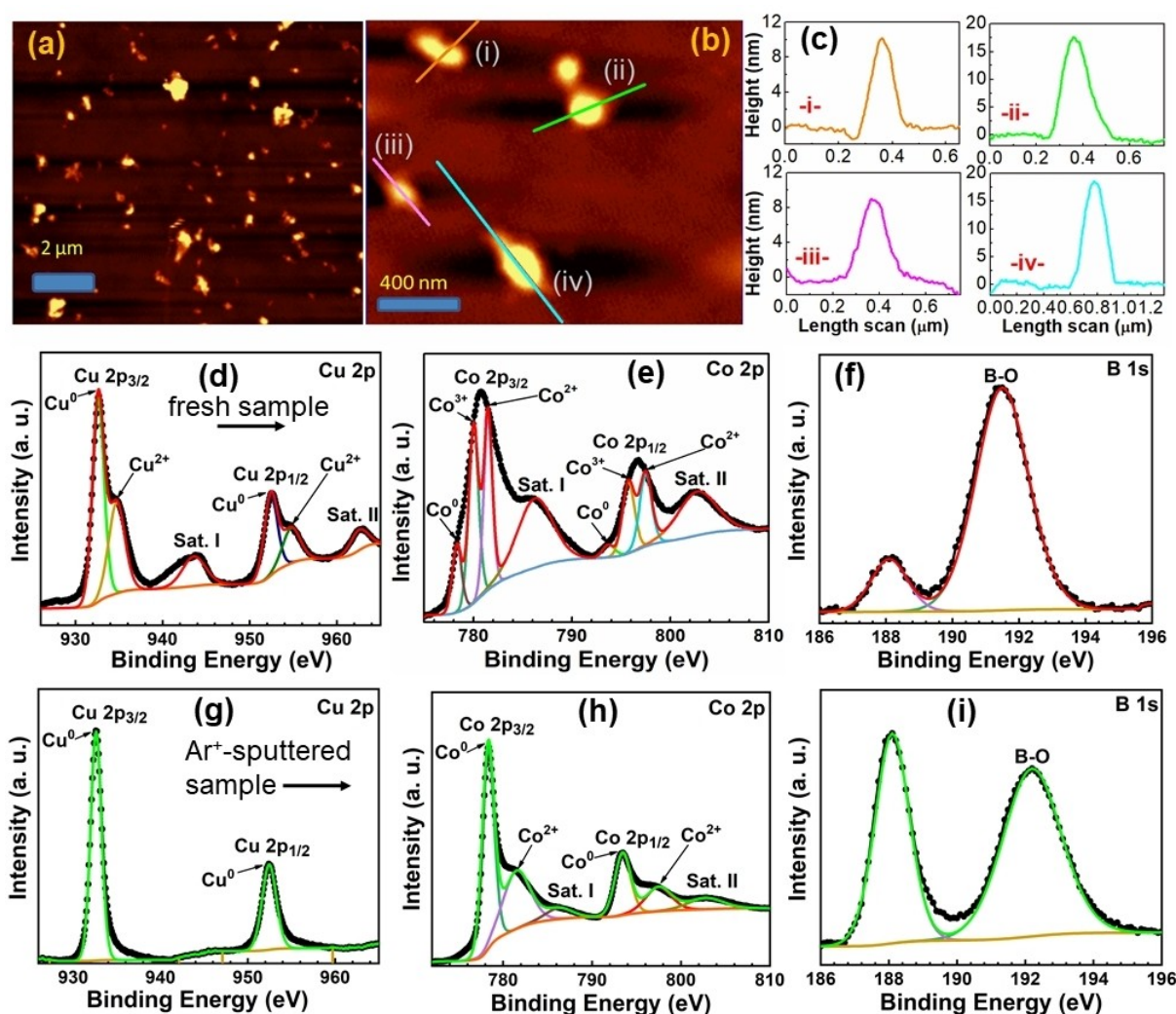
Figure 2. a) AFM image of CCB1. b) Line scanning of a very dilute sample to measure the thickness of the sheets, and c) corresponding height chart. High-resolution deconvoluted XPS spectra of as-synthesized and freshly Ar$^+$-sputtered CCB1 for d and g) Cu 2p, e and h) Co 2p, and f and i) B 1s, respectively.

the peak intensities of Co^{2+} were drastically reduced and the peak intensities of Co^0 were drastically enhanced (Figure 2h). The original B–O peak intensity is reduced and B^0 peak intensity is enhanced (Figure 2i). The in-situ sputter cleaning method presented here demonstrates the impurity oxides are restricted to the surface and these probably act as a protective layer against further degradation of the originally formed Cu^0–Co^0–B^0 alloy.

Electrochemical properties of Cu–Co–B samples

The electrochemical properties of CCB1, CCB2 and CCB3 were evaluated with a three-electrode system. At first cyclic voltammetry (CV) curves of all three samples and bare Ni-foam substrate measured at 5 mV s^{-1} within 0.0–0.45 V are compared in Figure 3(a). It shows a large integral area of battery type CV CCB1 over CCB2 and CCB3 samples. The obtained current density (integral area as well) for Ni-foam is negligible as compared to the alloy samples. Further comparison of galvano-

static charge-discharge (GCD) curves for the same working electrode (Figure 3b) at 5 A g^{-1} current density reveals CCB1 possesses the greatest discharge time among the samples and hence it has the largest specific capacitance. CV curves of CCB1 (Figure 3c) at various scan rates (5–100 mV s^{-1}) have four redox peaks corresponding to the reversible reactions shown in Figure S6.[10,11,19] The redox peaks are possible due to the oxidation and reduction of metal ions as Cu$^+$↔Cu^{2+} and Co^{2+}↔Co^{3+} in 6 M KOH, as corroborated from XPS analyses and the formation of the intermediates as shown in Figure S6. CV curves of CCB2 and CCB3 at various scan rates are given in Figure S7,8, respectively. For the same working electrode, the GCD curves of CCB1 (Figure 3d) are nearly symmetric during the charging-discharging cycles at different current densities (3–20 A g^{-1}), indicating good reversibility and good Coulombic efficiency (101.8% after 10000 cycles at 50 A g^{-1} current density). CCB1 offered best electrochemical results as compared to other two samples may be corroborated to its larger specific area and pore size (effective electrolyte and electrode inter-action) as compared to CCB2 and CCB3, and the optimum 1:2
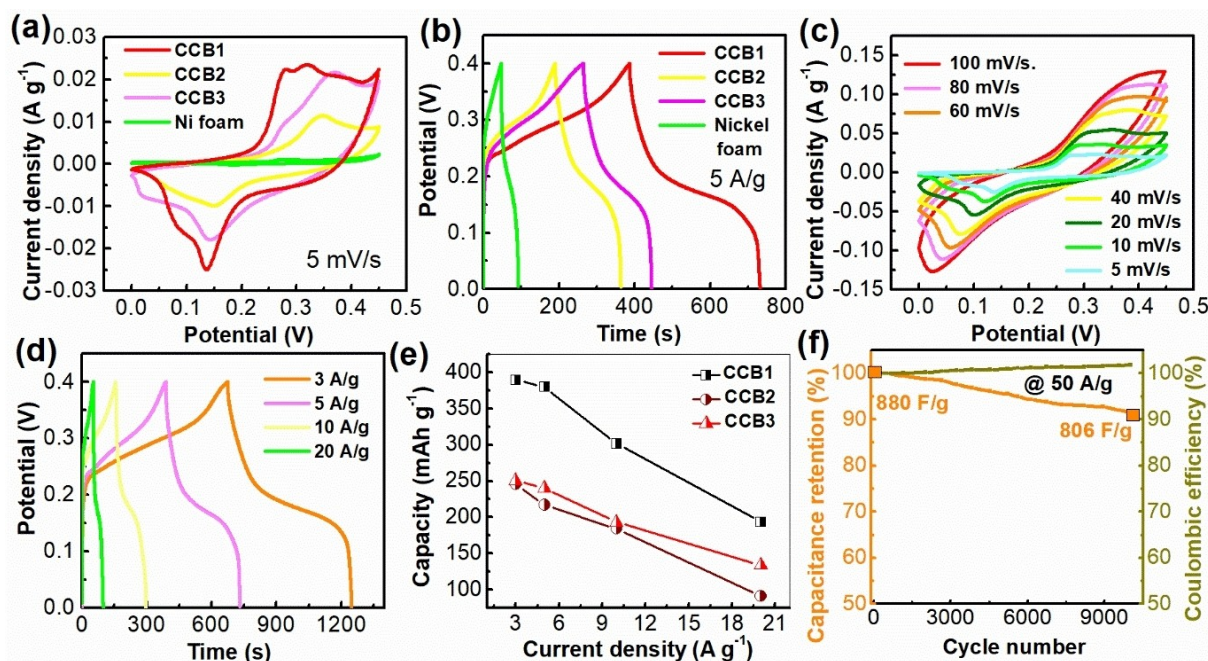
Figure 3. Electrochemical performance of Cu–Co–B cathodes. a) CV curves of CCB1, CCB2, CCB3 and bare Ni-foam. b) GCD curves all compositions along with bare Ni-foam. c and d) CV and GCD of CCB1 at different scan rates and current densities, respectively. e) Specific capacity curves at the different current density of CCB1, CCB2 and CCB3. f) Cycling life and columbic efficiency of CCB1 at 50 A g^{-1} up to 10000 cycles.

ratio of Cu and Co. See Figures S9 and S10 for GCD curves of CCB2 and CCB3 respectively.

To thoroughly study the electrochemical properties of Cu–Co–B, we studied further the influence of the chemical composition of Cu and Co for the electrochemical properties. For this, electrochemical impedance spectroscopy (EIS) measurements were performed. A very low charge transfer resistance (R_{ct}, 0.17 ohm cm^2) and total resistance (R, 1.85 ohm cm^2) is obtained for CCB1 sample from the Nyquist plots (Figure S11), which are significantly lower than other two compositions (Table S2). The obtained EIS data was further fitted using an equivalent electric circuit (as shown in insets of Figure S11), where R_b is the bulk, R_{ct} is the charge transfer resistance, C is the capacitance and W is the Warburg element. The higher conductivity corroborated to many factors, such as alloy structure with B rather than oxide or sulphide form, hybridization between valance orbital of transition metal and 2p orbital of boron, which raised the density of valance electrons.[11,20] The specific capacity values for the CCB1 electrode from Figure 3(d) are 389.2, 379.8, 301.5 and 193.5 mAh g^{-1} at the corresponding current densities of 3–20 A g^{-1}, respectively. The corresponding specific capacitance values are found to be 3503.6, 3418.3, 2713.2, 1742.0 F g^{-1} at the same current densities (Table S3). Notably, we have subtracted capacity value of bare Ni-foam substrate in all cases. The capacity values for CCB1 are much higher than the capacitance for the CCB2 and CCB3 at all the current densities (Figure 3e). As mentioned earlier, the higher efficiency of CCB1 may be corroborated to its larger specific area and pore size, and the optimum 1:2 ratio of Cu and Co. Cobalt is electrochemically more active than copper, hence 1:2 ratio gives the best synergistic effect of the metals in CCB1. Besides, when the current density raised from 3 to 20 A g^{-1}, the capacitance for the CCB1 electrode retained ~50% of its original capacity, depicting higher rate capability at high current density. The capacitance values for CCB1 are also higher in comparison to the similar materials (metal borides, spinels, metal hydroxides, etc.) reported previously, and compared in Table S4. Figure 3(f) shows that the CCB1 maintains 99% and 91% of capacitance retention after 3000 and 10000 cycles, respectively, suggesting excellent cycling stability even at 50 A g^{-1} current density. A portion of CCB1 sample was collected after the 10000 GCD cycles and characterized again to analyse phase, morphology and chemical structure of the alloy. Retention of nanosheet morphology after 10000 cycles is seen under TEM and FESEM imaging (Figure S12a and b). The sample remained amorphous as seen from post-cycled XRD pattern (Figure S13a). Moreover, high resolution XPS spectra (peaks) of Cu 2p, Co 2p and B 1s (Figure S13b–d) resemblance the original XPS spectra in Figure 2(d–f) of the fresh sample containing identical oxide peaks, confirming high stability of the material without further degradation and further surface oxidation.

To check the energy storage advantage of nanosheet morphology over spherical nanoparticles (NPs), we have synthesized CCB4. The agglomerated NPs (Figure S14a) offers smaller CV curves (Figure S14b) as well as lower discharge specific capacity as calculated from GCD curves (Figure S14c) compared to present nanosheet samples (Table S5). Moreover, R_b, R_{ct} and R values are also found to be higher than the nanosheet samples (Table S2), corroborating the importance of 2D morphology.

Batteries & Supercaps

Research Article
doi.org/10.1002/batt.202100314

**Chemistry
Europe**
European Chemical
Societies Publishing

The reaction kinetic features and charge storage mechanism were evaluated by analysing the internal connection between the current (i) and sweep rate (v), and with the help of low scan rate CVs of CCB1 (Figure S15a).[7c,21]

$$i = av^b \tag{1}$$

A straight-line fitting is obtained by taking log on both side of Equation (1), which gives rise to the slope b. This slope value gives information about dominated charge storage mechanism of the cell, whether it is surface controlled (if $b=1$) or diffusion-controlled process (if $b=0.5$). In the present case, the parameter b is calculated in Figure S15(b) from slope of the linear fittings ($\log i = \log a + b \log v$) and is found to be 0.8 for scan rate ≥ 10 mV s^{-1} and 0.9 for scan rate ≤ 10 mV s^{-1}; indicating a dominant surface-controlled faradaic procedure (extrinsic pseudocapacitance due to nanoscale CuCo$_2$B)^3 along with battery-type behaviour due to diffusion process coming under "transitional area".[22] The capacitive and diffusion-controlled contributions to the total capacity was calculated using:

$$i(V) = k_1 v + k_2 v^{1/2} \tag{2}$$

where $i(V)$ is the response current at a particular voltage V and $k_1 v$ and $k_2 v^{1/2}$ are capacitive and diffusion-controlled contributions, respectively. A dominant capacitive process is underlined from Figure 4a and this capacitive-controlled contribution occupies about 85.8%, 89.0%, 91.3%, 92.5% and 93.0% of the total capacity at 0.2, 0.4, 0.6, 0.8, and 1.0 mV s^{-1}, respectively (Figure 4b). This further suggests that the battery-type capacitive-controlled charge-storage mechanism is mainly surface 'extrinsic' pseudocapacitive faradaic reactions, which increases with the increase of the sweep rate.[5b] Furthermore, the overall charge (q) of the capacitor cell and the contributions from surface capacitive charge (q_c) were obtained by extrapolation of a linear plot of $1/q$ versus $v^{1/2}$ to $v=0$ (Figure S15c) and q versus $v^{-1/2}$ to $v=\infty$ (Figure S15d), respectively.[23] The overall charge is found to be 1951 C g^{-1} and the prominent surface capacitive charge contribution is found to be 1318 C g^{-1}. The diffusion-controlled charge (q_i) contribution is calculated to be

634 C g^{-1}. With the help of the bode plot (Figure S16), we measured the kinetics of fast reversible redox reaction in terms of response frequency (f_o) and response time (τ_o) from EIS analysis of CCB1. The response time is calculated by the reciprocal response time evaluated by the bode plot based on Miller's approach.[24] A very small value of τ_o (0.59 s.) indicated a very fast faradic reaction in Cu–Co–B.

Since, Cu–Co–B with higher Co ratio (i.e., CuCo$_2$B) shows best specific capacitance and lower resistance because of the optimized content of electrochemically more active Co, we further prepared three more control samples (Cu$_3$B, Co$_3$B and Cu$_{0.5}$Co$_{2.5}$B) using the same synthesis method and studied their CVs and GCDs (Figure S17). As expected, lowest capacity is observed for Cu$_3$B, however increasing Co:Cu ratio in Co$_3$B and Cu$_{0.5}$Co$_{2.5}$B is not found to increase charge storage capacity (Table S6). Thus, an optimized Cu to Co ratio is indeed necessary for the best charge storage behaviour.

Electrochemical performance of the CuCo$_2$B│[EMIM][BF$_4$] symmetric flexible device

The potential application capability of solvent-free CuCo$_2$B as a flexible supercapacitor was evaluated by assembling a symmetric device, where [EMIM][BF$_4$]:PVDF film was used as the electrolyte cum separator. The purpose of using the current [EMIM][BF4] ionic liquid as an electrolyte in the flexible device is that, it has high thermal and chemical stability, wide range of operating temperature range, a broad electrochemical potential stability window, high ionic conductivity at room temperature, and non-flammability, and these advantages are not offered by aqueous electrolytes in a flexible device.[18b,25] At first conductivity of the flexible cell was measured using EIS in a frequency range of 10^{-2} Hz–100 kHz (Figure 5a). The R_{ct} and R of the device are measured to be 7.64 and 30.95 ohm cm^2, respectively, which is higher than three-electrode measurement due to the presence of PVDF binder, GPPCS substrate and the geometry of the former configuration. This EIS plot is further fitted and the obtained equivalent circuit diagram is shown in upper inset of Figure 5(a). Here, R_b is the bulk, R_{ct} is the charge transfer resistance, CPE is constant phase element and W is the
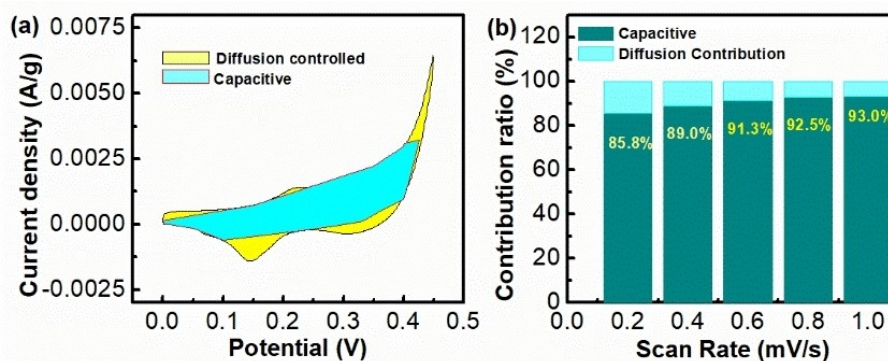

Figure 4. a) Separation of the capacitive and diffusion-controlled currents of CCB1 electrode at a scan rate of 5 mV s^{-1}. b) Relative contributions of the capacitive and diffusion-controlled charge storage processes at different scan rates.

Batteries & Supercaps

Research Article
doi.org/10.1002/batt.202100314

Chemistry
Europe
European Chemical
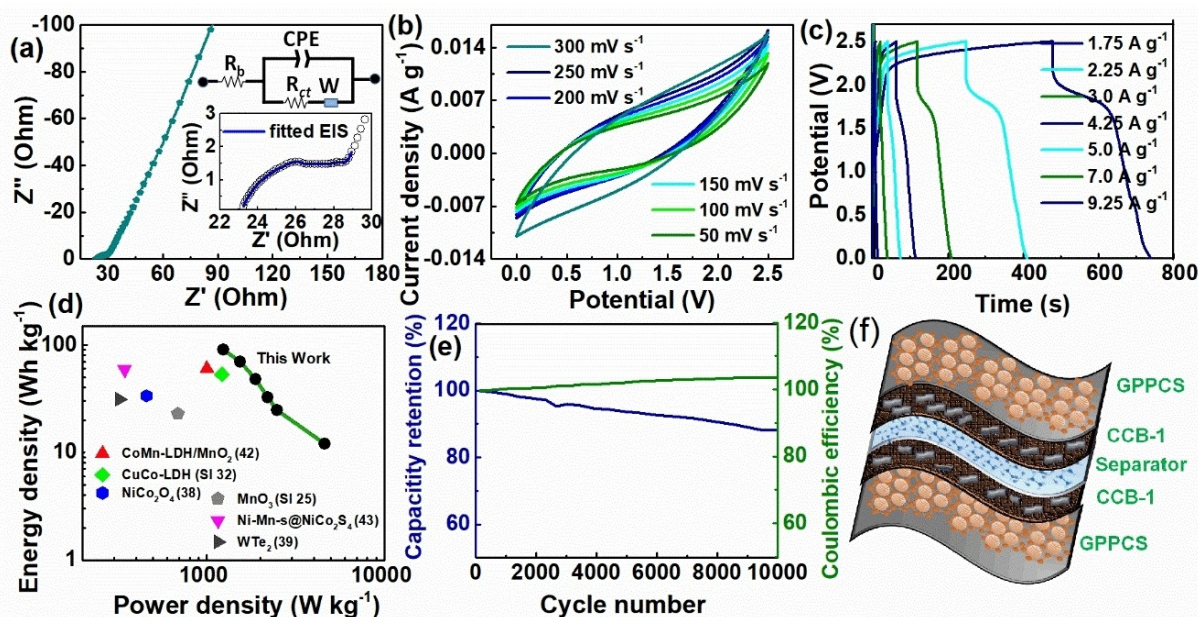Societies Publishing

Figure 5. The overall electrochemical performance of flexible device based on CCB1. a) Nyquist plot was obtained at room temperature. Inset: zoomed area and fitted plot of high frequency region EIS curve and the equivalent circuit diagram. b) CV curve obtained at different scan rate for flexible. c) GCD cycles were recorded at various current densities. d) Ragone plot for flexible device and comparison with other flexible devices (reference number). e) The cycling performance of the flexible device was measured at a current density of 9.25 A g^{-1} up to 10000 cycles. f) Schematic illustration of the assembled symmetric flexible cell and the components.

Warburg element. The fitting reveals that linearly raised imaginary part of impedance at low frequency is the Warburg diffusion process for the ion diffusion process in the electrode material for the capacitive behaviour of the cell. At high frequency region a semicircle fitting gives R_b and R_{ct}. Figure 5(b) shows the reversible CV curves measured within the full potential window (0–2.5 V) at different sweep rates. The GCD curves of the **CuCo$_2$B**|[EMIM][BF$_4$] SC at different current densities (1.75–9.25 A g^{-1}) are shown in Figure 5(c) and the capacity values were calculated to be 289.2, 222.5, 153.7, 104.0, 78.9, 45.6 and 38.3 mAh g^{-1} at the given current densities, respectively (see Table S7 for C_{sp} values)

The **CuCo$_2$B**|[EMIM][BF$_4$] flexible device delivered a whipping energy density of 90.3 Wh kg^{-1} at the power density of 1240.3 W kg^{-1} (Ragone plot, Figure 5d) and which can reach up to 4623.6 W kg^{-1} (Table S7). Present values are extremely on the higher side as seen from the comparative data on a few flexible devices in Figure 5(d). Another important parameter is the excellent cycling stability of the symmetric SC. The flexible device retained 89% of its original capacitance after 10000 cycles at 9.25 A g^{-1} (Figure 5e). The device retained almost 94% of its original capacitance till 5000 cycles and after that the retention is reduced to 89%. Notably, Coulombic efficiency remains almost constant till 5000 cycles and increased to nearly 104% after 10000 cycles. A high coulombic efficiency, >100%, could be due to many factors as described in literature, such as formation of net negative charge on the surfaces, due to the decomposition of electrolyte in discharging process (additional electrode reaction), blocking of pores of the electrode materials for electrolytes, etc. However, it is not clear which one is responsible for present result. These parameters (capacity,

energy density, cycling stability) demonstrate superior performance and a clear and significant improvement of the **CuCo$_2$B**|[EMIM][BF$_4$] SC compared with those previously reported state-of-the-art flexible and/or 2-electrode devices, such as, TM-LDHs, NiCo$_2$O$_4$, RuO$_2$, TMB, Bi NSs, etc.[25,26] The detailed comparison is presented in Table S8.

These charge storage characteristics of CCB1 flexible device are also compared with flexible devices fabricated from CCB2 and CCB3 (Figure S18). It is found that, the specific capacitance offered by CCB2 (244.8 F g^{-1}) and CCB3 (281.1 F g^{-1}) devices is lower than CCB1 (416.5 F g^{-1}) based flexible device. Moreover, the conductivity of the devices is found to be in the inverse order.

The potential applicability of the fabricated flexible device was further studied for higher potential window stability and bending performance. Figure 6(a) shows the CV curves for symmetric SC at scan rates 300 mV s^{-1} measured in the full different potential window (0–2.5 V). CV curves retained a similar symmetric shape, confirming the operable low voltage (1.0 V) as well as high voltage (2.5 V). The flexible device also offered sustainable device performance in bending condition. GCD cycles were measured at 5.0 A g^{-1} current density and 2.5 V potential to evaluate the capacitance of the flexible cell at different bending angles (0–180°, see Figure 6b). The capacity values were calculated to be 78.9, 78.7, 77.3, 74.9, 72.3, and 70.0 mAh g^{-1} at the bending angle of 0, 45, 60, 90, 135, and 180°, respectively (Figure 6c). The corresponding specific capacitance values at 0–180° are depicted in Table S9. This demonstrates superior performance of the CuCo$_2$B NS based flexible SC, which also took care the issue of electrolyte evaporation in long run, and leakage of electrolyte and
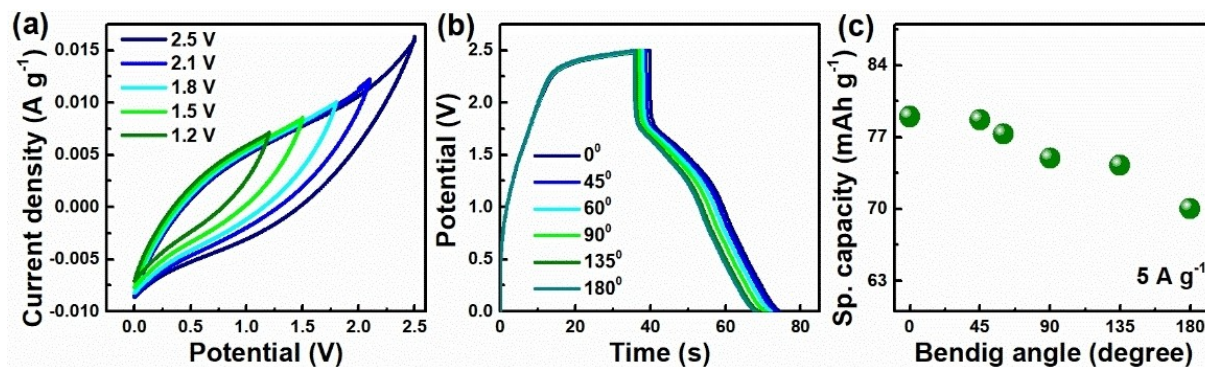
Figure 6. The electrochemical performance of the CCB1 based flexible device to ensure its flexibility. a) Cyclic voltammograms of flexible device at different potential window were recorded at scan rate of 300 mV s^{-1}. b) Galvanostatic charge-discharge cycles were obtained at various bending angle from 0–180° at current density of 5.0 A g^{-1} and c) the obtained capacitance plot as a function of bending angle at current density 5.0 A g^{-1}.

electrode shortening issues. Thus, all these combined parameters and the outstanding results warrant the excellence and novelty of the present material as well the all-solid-state symmetric flexible SC.

Conclusion

In summary, we have synthesized novel Cu−Co−B alloy composition and its nanosheets by an efficient one pot and low-cost chemical reduction method. The alloy NSs are 8–16 nm thick and amorphous in nature and proved to be a special attraction in the SC device. The SC obtained a high specific capacity of 389.2 mAh g^{-1} (3503.6 F g^{-1}) and a 99% and 91% retention rate after 3000 and 10000 cycles, respectively. An all-solid state flexible symmetric SC device demonstrated a high energy density of 90.2 Wh kg^{-1}, specific capacity (289.2 mAh g^{-1}), and superlong cycling stability (89%) and Coulombic efficiency (104%) over 10000 GCD cycles. The device retained these performance parameters almost intact at various bending conditions (0–180°) and at high operating potential (2.5 V). The new Cu−Co−B TMB composition, its new cost-effective synthesis method, alloy structure, high surface area nanosheet morphology, and redox properties; are expected to provide a way to better functional materials in energy storage and electrocatalysis, and a miniature flexible device.

Experimental Section

Synthesis of amorphous Cu−Co−B nanosheets. In a typical procedure, 0.5 mmol of copper acetate and 1 mmol of cobalt acetate was dissolved in 30 mL of double-distilled water. The solution was stirred for 10 min to form a homogeneous mixture. Then 2.3 mL of 1.0 M KOH was added to the above solution under continuous stirring for another 5–10 min to adjust the pH at 12 and observed that the solution became turbid and dark pink in color. After that 6 mL of 0.9 M NaBH$_4$ solution (reducing agent as well as source of boron) was added drop wise to the previous solution and stirred for another 40 min. The resultant black coloured product was washed three times with distilled water and

two times by ethanol followed by drying at 60 °C for 15 h. The as-synthesised product was dispersed in ethanol for further activity. Different compositions of Cu:Co were also synthesised by fixing the total amount of metal acetates to be 1.5 mmol (Cu:Co molar ratio of 1:2, 2:1, 1:1; the compositions were coded as CCB1, CCB2 and CCB3 respectively). For comparison, Cu−Co−B nanoparticles (CCB4) of size 5–10 nm was also synthesised by similar synthesis method by adding NaBH$_4$ instantaneously after adding KOH.

Electrochemical measurements. The working electrode was prepared by mixing Cu−Co−B, acetylene black and PVDF at a mass ratio of 75:15:10 in acetone and stirring for 6 h to make a homogeneous slurry. Then, the slurry was drop casted on a cleaned Ni-foam substrate (1 cm×3 cm) and dried at 50 °C for 6 h. The mass loading on the substrate is calculated to be 0.94 mg cm^{-2}. A Pt sheet (1 cm^2) and an Ag/AgCl (aq.) electrode were used as counter electrode and reference electrode, respectively, and 6 M KOH aqueous solution was used as the electrolyte in the three-electrode study. All electrochemical operations were performed on a 660E, CHI Instrument (USA) electrochemical workstation.

Fabrication of flexible symmetric supercapacitor cell. At first, a flexible graphite powder-polymer composite sheet (GPPCS) substrate was prepared as reported earlier, which is used as a conducting substrate to the deposited electrode material. A Cu−Co−B slurry was made in ethanol and drop casted on GPPCS. The flexible electrode was dried at 50 °C for 12 h. The weight of the transferred electrode material (mass loading) was found to be 1.12 mg on 1 cm×1 cm substrate. A 5:1 ratio of [EMIM][BF$_4$]:PVDF was used to form the flexible ionic liquid electrolyte cum separator. The mixture was dissolved into a suitable amount of acetone in a beaker, sonicated for 1 h followed by stirring for 24 h, poured into a flat glass dish and dried (solidified) at 25 °C for 4–5 days inside a glovebox, respectively. To fabricate the flexible cell (1 cm×1 cm or 1 cm ×3 cm), this electrolyte cum separator sheet was sandwiched between two electrode sheets and dried this final cell in an oven at 50 °C for 30 h.

The specific capacity (C_{sc}) and mass-specific capacitance (C_{sp}) were obtained based on GCD experiments following Equations (3) and (4):

$$C_{sc} = \frac{2i \int \Delta V dt}{m \Delta V} \tag{3}$$

$$C_{sp} = \frac{2i \int \Delta V dt}{m \Delta V^2} \tag{4}$$

Batteries & Supercaps

Research Article
doi.org/10.1002/batt.202100314

Chemistry
Europe
European Chemical
Societies Publishing

where m is the mass of single electrode material without substrate, i is the discharge current, $\triangle V$ is the potential window and $\int \Delta V dt$ is the integral area of the discharge process.

The gravimetric energy density (E, Wh kg^{-1}) and power density (P, W kg^{-1}) of the cells were calculated by using the Equations (5) and (6).

$$E = \frac{1000 \times C_{sp} \times \Delta V^2}{3600 \times 2} \tag{5}$$

$$P = \frac{3600 \times E}{\Delta t} \tag{6}$$

Acknowledgements

Conflict of Interest

The authors declare no conflict of interest.

Data Availability Statement

Research data are not shared.

[1] J. Liu, J. Wang, C. Xu, H. Jiang, C. Li, L. Zhang, J. Lin, Z. X. Shen, *Adv. Sci.* **2017**, *5*, 1700322.

[2] a) A. Eftekhari, *J. Mater. Chem. A* **2018**, *6*, 2866–2876; b) Z. Shen, Z. Tang, C. Li, L. Luo, J. Pu, Z. Wen, Y. Liu, Y. Ji, J. Xie, L. Wang, Y. Yao, G. Hong, *Adv. Energy Mater.* **2021**, *11*, 2102055.

[3] a) P. Simon, Y. Gogotsi, B. Dunn, *Nat. Mater. Science* **2014**, *343*, 1210–1211; b) Y. Gogotsi, R. M. Penner, *ACS Nano* **2018**, *12*, 2081–2083; c) J. Zhao, Y. Zhang, X. Zhao, R. Wang, J. Xie, C. Yang, J. Wang, Q. Zhang, L. Li, C. Lu, Y. Yao, *Adv. Funct. Mater.* **2019**, *29*, 1900809.

[4] a) X. Li, D. Du, Y. Zhang, W. Xing, Q. Xue, Z. Yan, *J. Mater. Chem. A* **2017**, *5*, 15460–15485; b) M. A. A. M. Abdah, N. H. N. Azman, S. Kulandaivalu, Y. Sulaiman, *Mater. Des.* **2020**, *186*, 108199; c) X. Zhang, G. Qu, Z. Wang, G. Xiang, S. Hao, X. Wang, X. Xu, W. Ma, G. Zhao, *Chin. Chem. Lett.* **2021**, *32*, 2453–2456; d) G. Qu, Z. Wang, X. Zhang, S. Zhao, C. Wang, G. Zhao, P. Hou, X. Xu, *Chem. Eng. J.* **2021**, *429*, 132406; e) K. Zhou, W. Zhou, L. Yang, J. Lu, S. Cheng, W. Mai, Z. Tang, L. Li, S. Chen, *Adv. Funct. Mater.* **2015**, *25*, 7530–7538; f) N. Zhang, Y. Li, J. Xu, J. Li, B. Wei, Y. Ding, I. Amorim, R. Thomas, S. M. Thalluri, Y. Liu, G. Yu, L. Liu, *ACS Nano* **2019**, *13*, 10612–10621.

[5] a) C. Choi, D. S. Ashby, D. M. Butts, R. H. DeBlock, Q. Wei, J. Lau, B. Dunn, *Nat. Revi. Mater.* **2019**, *5*, 5–19; b) Y. Jiang, J. Liu, *Energy Environ. Sci.* **2019**, *2*, 30–37; c) C. Li, X. Sun, Y. Yao, G. Hong, *Mater. Today Nano* **2021**, *13*, 100105.

[6] a) M. I. Khan, F. Bibi, M. M. Hassan, N. Muhammad, M. Tariq, A. Rahim, *Flex. Supercap. Nanoarchit.* **2021**, 263–275; b) G. Qu, P. Sun, G. Xiang, J. Yin, Q. Wei, C. Wang, X. Xu, *Appl. Mater. Res.* **2020**, *20*, 100713; c) G. Xiang, Y. Meng, G. Qu, J. Yin, B. Teng, Q. Wei, X. Xu, *Sci. Bull.* **2020**, *65*, 443–451; d) Y. Shao, Y. Zhao, H. Li, C. Xu, *ACS Appl. Mater. Interfaces* **2016**, *8*, 35368–35376.

[7] a) K. S. Kumar, N. Choudhary, Y. Jung, J. Thomas, *ACS Energy Lett.* **2018**, *3*, 482–495; b) P. Nakhanivej, Q. Dou, P. Xiong, H. S. Park, *Acc. Chem. Res.* **2021**, *2*, 86–96; c) J. Cao, T. Zhou, Y. Xu, Y. Qi, W. Jiang, W. Wang, P. Sun, A. Li, Q. Zhang, *ACS Nano* **2021**, *15*, 2707–2718.

[8] a) L. Li, Z. Deng, L. Yu, Z. Lin, W. Wang, G. Yang, *Nano Energy* **2016**, *27*, 103–113; b) X. Zhang, L. Hou, A. Ciesielski, P. Samorì, *Adv. Energy Mater.* **2016**, *6*, 1600671.

[9] W. Zhang, X. Zhang, Y. Tan, J. Wu, Y. Gao, B. Tang, Y. Wang, *New J. Chem.* **2014**, *38*, 4666–4669.

[10] R. Chen, L. Liu, J. Zhou, L. Hou, F. Gao, *J. Power Sources* **2017**, *341*, 75–82.

[11] Q. Meng, W. Xu, S. Zhu, Y. Liang, Z. Cui, X. Yang, A. Inoue, *Electrochim. Acta* **2019**, *296*, 198–205.

[12] Q. Wang, Y. Luo, R. Hou, S. Zaman, K. Qi, H. Liu, H. S. Park, B. Y. Xia, *Adv. Mater.* **2019**, *31*, 1905744.

[13] W. Wang, J. Zhang, T. Li, S. Wang, *RSC Adv.* **2020**, *10*, 43109–43116.

[14] a) S. Gupta, N. Patel, R. Fernandes, R. Kadrekar, A. Dashora, A. K. Yadav, D. Bhattacharyya, S. N. Jha, A. Miotello, D.C. Kothari, *Appl. Catal. B* **2016**, *192*, 126–133; b) H. Han, Y. R. Hong, J. Woo, S. Mhin, K. M. Kim, J. Kwon, H. Choi, Y. C. Chung, T. Song, *Adv. Energy Mater.* **2019**, *9*, 1803799; c) D. Dong, X. Xu, C. Ma, L. Gong, L. Su, J. Wang, *Int. J. Hydrog.* **2020**, *45*, 4545–4555.

[15] Y. Chen, *Catal. Today* **1998**, *44*, 3–16.

[16] a) D. G. Tong, X. Han, W. Chu, H. Chen, X. Y. Ji, *Mater.* **2008**, *43*, 1327–1336; b) K. T. Møller, A. S. Fogh, M. Paskevicius, J. Skibsted, T. R. Jensen, *Phys. Chem. Chem. Phys.* **2016**, *18*, 27545–27553.

[17] J. F. Moulder, W. F. Stickle, P. E. Sobol, K. D. Bomben, Handbook of X-ray Photoelectron Spectroscopy, Ed. Chastain, J. Perkin-Elmer Corporation, Physical Electronics Division, Minnesota 55344 USA, **1992**.

[18] a) M. Chauhan, K. P. Reddy, C. S. Gopinath, S. Deka, *ACS Catal.* **2017**, *7*, 5871–5879; b) L. Kumar, P. K. Boruah, S. Borthakur, L. Saikia, M. R. Das, S. Deka, *ACS Appl. Nano Mater.* **2021**, *4*, 5250–5262.

[19] Y. Chen, T. Zhou, L. Li, W. K. Pang, X. He, Y. N. Liu, Z. Guo, *ACS Nano* **2019**, *13*, 9376–9385.

[20] R. Caputo, F. Guzzetta, A. Angerhofer, *Inorg. Chem.* **2010**, *49*, 8756–8762.

[21] H. S. Kim, J. B. Cook, H. Lin, J. S. Ko, S. H. Tolbert, V. Ozolins, B. Dunn, *Nat. Mater.* **2016**, *16*, 454–460.

[22] V. Augustyn, J. Come, M. A. Lowe, J. W. Kim, P. L. Taberna, S. H. Tolbert, H. D. Abruña, P. Simon, B. Dunn, *Nat. Mater.* **2013**, *12*, 518–522.

[23] a) S. Ardizzone, G. Fregonara, S. Trasatti, *Electrochim. Acta* **1990**, *35*, 263–267; b) J. Liu, J. Wang, C. Xu, H. Jiang, C. Li, L. Zhang, J. Lin, Z. X. Shen, *Adv. Sci.* **2017**, *5*, 1700322; c) P. Simon, Y. Gogotsi, *Nat. Mater.* **2020**, *19*, 1151–1163.

[24] a) P. Tamilarasan, S. Ramaprabhu, *Energy* **2013**, *51*, 374–381; b) J. Huang, Z. Li, B. Y. Liaw, J. Zhang, *J. Power Sources* **2016**, *309*, 82–98.

[25] L. Kumar, P. K. Boruah, M. R. Das, S. Deka, *ACS Appl. Mater. Interfaces* **2019**, *11*, 37665–37674.

[26] a) P. Yu, W. Fu, Q. Zeng, J. Lin, C. Yan, Z. Lai, B. Tang, K. Suenaga, H. Zhang, Z. Liu, *Adv. Mater.* **2017**, *29*, 1701909; b) H. Sheng, X. Zhang, Y. Ma, P. Wang, J. Zhou, Q. Su, W. Lan, E. Xie, C. J. Zhang, *ACS Appl. Mater. Interfaces* **2019**, *11*, 8992–9001; c) B. Yang, X. Li, Y. Cheng, S. Duan, B. Zhao, W. Yi, C. Wang, H. Sun, Z. Wang, D. Gu, S. Chen, X. Liu, *J. Mater. Chem. C* **2020**, *8*, 12314–12322; d) Y. Zhao, J. He, M. Dai, D. Zhao, X. Wu, B. Liu, *J. Energy Chem.* **2020**, *45*, 67–73; e) L. Wan, Y. Yuan, J. Liu, J. Chen, Y. Zhang, C. Du, M. Xie, *Electrochim. Acta* **2021**, *368*, 137579.